Journal of Advanced Environmental Research and Technology

jaert.modares.ac.ir

Numerical Study of the Aerodynamic Performance of a Brimmed Diffuser Augmented Offshore Wind Turbine across a Range of Tip Speed Ratios

Mamouri, Amir Reza.[1,*]

[1] Department of Mechanical Engineering, Technical and Vocational University (TVU), Tehran, Iran[2] Department of KIT-Kalaignarkarunanidhi Institute of Technology

Article info

Received 2024-08-26
Revised 2024-10-20
Accepted 2024-02-21

Abstract

This study presents a comprehensive CFD assessment of a brimmed diffuser augmented offshore wind turbine (BDAWT) versus a conventional three-blade horizontal axis offshore wind turbine (HAWT) across a tip speed ratio (TSR) range of 4–10. High-fidelity steady RANS simulations employing the SST k–ω turbulence model were conducted, with a rigorous mesh independence verification using up to 2.7 million cells. We extracted global performance metrics, namely the power coefficient (C_P), as well as detailed local flow data: axial velocity and static-pressure profiles on four characteristic cross sections (upstream of the rotor, diffuser throat, diffuser outlet vertical plane, and diffuser outlet horizontal plane), along with the corresponding velocity ratios. Compared with the baseline HAWT, the brimmed diffuser pre-accelerates the core flow by up to ~25%, induces a pronounced low-pressure suction region at the diffuser throat, and narrows the downstream wake. These effects collectively raise the peak C_P from 0.39 to 0.59 and shift the optimal TSR from 7 to 8. Furthermore, boundary layer separation on the blades is delayed in the BDAWT, and the local velocity ratio exceeds unity at the diffuser exit, confirming sustained flow acceleration through the rotor. The detailed pressure distributions and wake recovery trends provide quantitative guidance for optimizing diffuser geometry and brim angle. Our results lay a solid foundation for subsequent experimental validation and facilitate the practical deployment of high-efficiency diffuser-augmented offshore wind turbines in real-world renewable energy applications.

Keywords: Brimmed diffuser augmented offshore wind turbine (BDAWT); Horizontal axis offshore wind turbine (HAWT); Tip speed ratio (TSR); Computational fluid dynamics (CFD); Offshore wind energy

Keywords

.
.
.
.
.

* Corresponding: authoramirelmir3000@yahoo.com

DOI: ……..

1. Introduction

As global energy demand continues to rise and the imperative to reduce carbon emissions intensifies, offshore wind turbines have emerged as a key technology for large-scale renewable power generation. By being sited on fixed or floating platforms in areas of stronger, more consistent winds, these systems can produce substantial electricity; however, they also face challenges in aerodynamic efficiency, noise generation, and operational stability at low wind speeds. To address these limitations, diffuser augmented or shrouded configurations, often called "wind lens" turbines, enclose the rotor within a brimmed, converging-diverging duct. This arrangement guides and accelerates the incoming flow before it reaches the blades, while enhanced suction at the diffuser outlet increases mass-flow entrainment and mitigates tip-vortex losses [1–4].

The theoretical ceiling for wind-turbine efficiency was established by Betz in 1920, who showed via one-dimensional momentum theory that no rotor can extract more than 59.3% of the wind's kinetic energy [5]. Building on this foundation, Paraschivoiu compiled aerodynamic principles and blade design guidelines for Darrieus vertical-axis machines, while Igra conducted early R&D on shrouded configurations, demonstrating that a duct can indeed induce additional flow through the rotor [6,7]. Practical validation in marine turbines began much later with Cresswell et al. [8], who fitted a converging-diverging diffuser around a tidal stream turbine and achieved up to 30% power gains along with altered wake recovery under yawed flow. In the same year, Shahsavarifard and Bibeau [9] reported as much as 90% improvement in hydrokinetic rotor power by adding flanged shrouds to mitigate tip losses.

Subsequent CFD studies refined these insights: El-Zahaby et al. [10] identified optimal flange angles for maximizing mass flow entrainment and C_P in a shrouded wind turbine, while Dighe et al. [11] demonstrated how duct geometry influences aerodynamic performance across TSRs in ducted turbines. Ghenai et al. [12] used RANS simulations to show that an optimized shroud geometry can delay stall on the rotor and improve pressure recovery in the wake. Recent work has also focused on practical deployment challenges. Refaie et al. [13] compared various Archimedean spiral diffusers to pinpoint geometries yielding the best wake control and C_P enhancement. Katooli and Noorollahi [14] critically reviewed scale-up and integration issues in shrouded turbines, Hameed et al. [15] optimized small-scale spiral shrouds for low-wind regimes, and Du et al. [16] quantified how support-structure interference can reduce a diffuser-augmented turbine's power coefficient by over 4% in offshore settings. Meanwhile, Mamouri et al. [17–19] examined unsteady aerodynamic effects on the SD7062 airfoil under pitching (dynamic stall) conditions, replicating realistic offshore turbine blade motions, and elucidated the transient loadings and performance of wind turbine airfoils. A number of recent studies published in this field can be summarized as follows. Katooli and Noorollahi[20] presented a critical review of shrouded wind turbine research, emphasizing the aerodynamic role of diffuser geometry, flow acceleration mechanisms, and performance limitations at large scales. Refaie et al. [21] and Hameed et al. [22] investigated novel diffuser geometries and optimization strategies, demonstrating that diffuser shape strongly affects wake behavior, pressure recovery, and efficiency enhancement. From a theoretical perspective, Watanabe and Ohya [23] developed a momentum-based model for brimmed diffuser turbines, clarifying the physical basis of diffuser-induced mass flow augmentation. In addition, Du et al. [24] examined offshore diffuser augmented turbines and showed that support structures can noticeably influence aerodynamic performance. These recent studies highlight the importance of diffuser rotor interaction and operating conditions, providing the context and motivation for the present investigation.

Within this rich context, the present study employs high-fidelity CFD to compare the aerodynamic performance of a brimmed diffuser-augmented offshore wind turbine (BDAWT) against a baseline three-blade offshore HAWT over TSR = 4–10. We analyze axial velocity, static pressure, and velocity ratio profiles at multiple cross-sections to quantify the diffuser's impact on the turbine's power coefficient and overall efficiency. The findings deliver actionable guidance for diffuser geometry optimization and optimal TSR selection, advancing the design of high-efficiency offshore wind turbines. The novelty of this study lies in its systematic, momentum-based interpretation of diffuser-augmented wind turbine aerodynamics. By performing a controlled, TSR-resolved CFD comparison between a conventional HAWT and a brimmed diffuser-augmented turbine using an identical rotor, the present work quantitatively links classical axial induction theory with diffuser-induced pressure gradients, flow acceleration, and mass-flow augmentation. This unified approach reveals an extended high-efficiency operating range and a shifted optimal tip speed ratio for the diffuser augmented turbine, providing physical insight beyond peak power enhancement and advancing the understanding of wind-lens turbine performance under realistic operating conditions.

2. Methodology

2.1 Geometry and Computational Domain

A three-bladed rotor of diameter D = 1.16 m, using SD7062 airfoil profiles (blade length L = 0.5 m), was used in both the HAWT and BDAWT configurations. In the HAWT, the blades were fixed at a pitch angle (root chord angle) of 4°. In the BDAWT, the same rotor is enclosed by a coaxial converging-diverging diffuser (shroud). The diffuser is defined by throat diameter Dth=1.17 m, inlet diameter Din=1.43 m, outlet diameter Dout=1.79 m, shroud length Lshroud=1.46 m, and wall thickness t=0.05 m. A circular brim of height hbrim=0.5 m was added around the diffuser's exit periphery to enhance suction and stabilize the outflow (see Fig. 1 for the HAWT and BDAWT geometries).

The computational domain was a large cylindrical volume of diameter 6D and length 12D, as illustrated in Fig. 2. The rotor hub was located 3D downstream of the inlet plane, leaving approximately 9D of space downstream of the rotor to capture the wake development before the outlet boundary. Boundary conditions were applied as follows: a uniform steady wind velocity U_∞ was prescribed at the inlet (upstream face of the cylinder), a pressure-outlet condition (static pressure equal to ambient) at the downstream end, and symmetric (frictionless slip) conditions on the lateral cylindrical surface to emulate an open atmosphere. This setup minimizes artificial blockage and reflections, ensuring that the flow around the turbine can develop naturally.

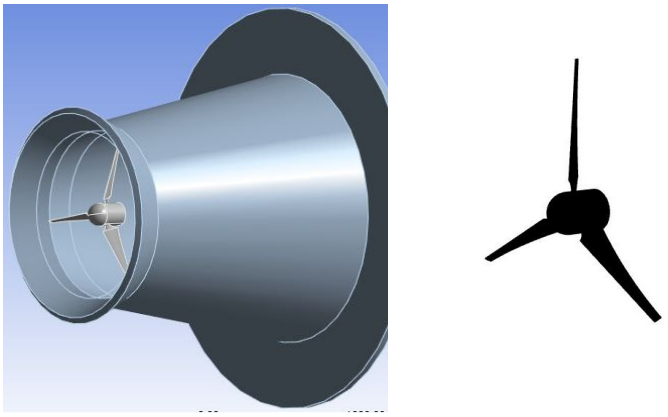

BDAWT HAWT

Fig. 1. Geometries of the designed HAWT and BDAWT.

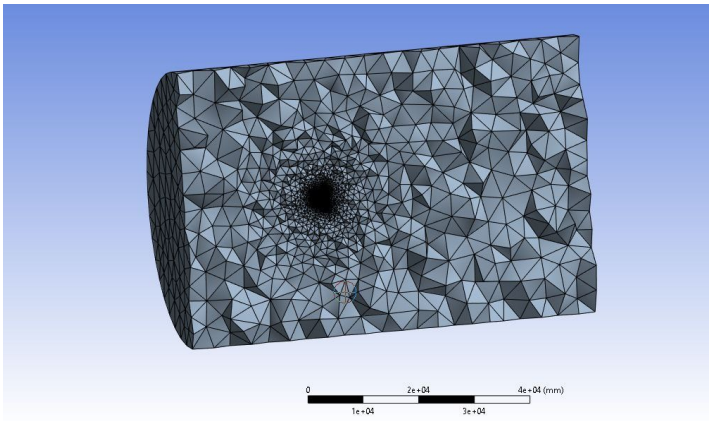

Fig. 2. Computational domain and the generated mesh within it

2.2 Mesh Generation and Grid Independence

An unstructured tetrahedral mesh was generated in ANSYS Workbench (Meshing module) for each configuration (Fig. 3). Fine mesh refinement was applied near the blades and diffuser surfaces: five prism layers (growth ratio 1.2) were extruded from all solid walls (blade surfaces and inner diffuser wall) to resolve the boundary layers, targeting y+<1 on those surfaces. The final grid for the BDAWT case comprised approximately 896,000 nodes and 2,725,900 cells (elements). A similar mesh density was used for the HAWT (without the diffuser).

To ensure that the simulation results were independent of grid resolution, a grid-independence study was carried out using four progressively refined meshes of roughly 150,000, 500,000, 1,400,000, and 2,700,000 cells. The axial velocity profiles along key lines (described later) were monitored for changes with mesh refinement. Differences in axial velocity (at mid-span in front of the rotor, and at the diffuser throat) were less than 0.1% when increasing mesh density from ~1.4 million to ~2.7 million cells. Therefore, the 2.7 million-cell mesh was deemed sufficiently fine (grid-independent) and was adopted for all subsequent simulations (Fig. 4 shows representative profile comparisons confirming this convergence).

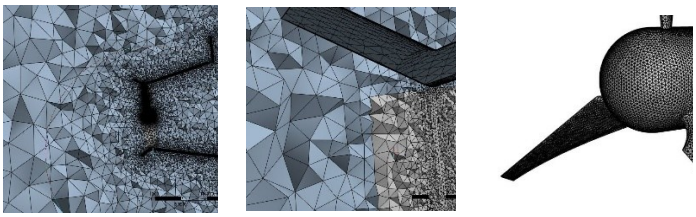

Fig. 3. Unstructured tetrahedral mesh generated using ANSYS Meshing Workbench

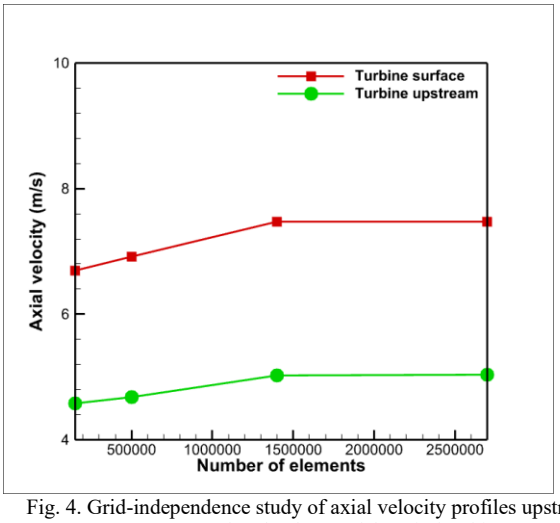

Fig. 4. Grid-independence study of axial velocity profiles upstream of the rotor and at the throat of the wind turbine.

2.3 Validation of the Numerical Model

Since no experimental data were available for the specific operating conditions investigated in this study, the numerical model was validated using the experimental results of Ohya et al. [3], which involved a horizontal-axis wind turbine with a rotor diameter of 1.0 m, throat diameter of 1.02 m, brim height of 0.1 of throat diameter, shroud length to throat diameter ratio of 0.225, and outlet to throat area ratio of 1.119, tested in a wind tunnel at an inlet velocity of 8 m/s. Wind tunnel blockage effects in the Ohya experiment likely caused an acceleration of the flow around the model, leading to slightly higher measured Cp values compared to free field conditions used in the present simulations. Fig. 5 shows that, for both HAWT and BDAWT, the simulated and experimental C_p –TSR trends agree well, with differences C_p of less than ~10%. In both analyses, the C_p values at low TSR are almost identical, indicating the limited effectiveness of the diffuser in this range, while at high TSR, the C_p The BDAWT is nearly twice that of the HAWT, demonstrating the diffuser's strong influence at higher TSR values; in this regard, the experimental and numerical results are in close agreement. Larger deviations at higher TSR values are attributed to three-dimensional flow effects, possible separation on the blades, tip vortex behavior, turbulence model limitations, and the absence of blockage in the numerical domain. The shift of the optimal TSR from ≈ 4 in Ohya's results to ≈ 5 in the present study is mainly due to geometric differences and the use of the SD7062 airfoil, which has higher lift at low angles of attack and different stall characteristics, along with variations in shroud length and inlet outlet profiles. The numerical results show good qualitative agreement with the experimental wind lens turbine data reported by Ohya and Karasudani. Although differences in diffuser length, brim height, and rotor design lead to different absolute performance levels and optimal TSR values, the dominant trends, namely, significant power augmentation and an upward shift in the optimal operating point, are consistent with both experimental and numerical studies reported in the literature. These differences highlight the strong influence of diffuser geometry and rotor diffuser matching on performance and underscore the need for geometry-specific optimization.

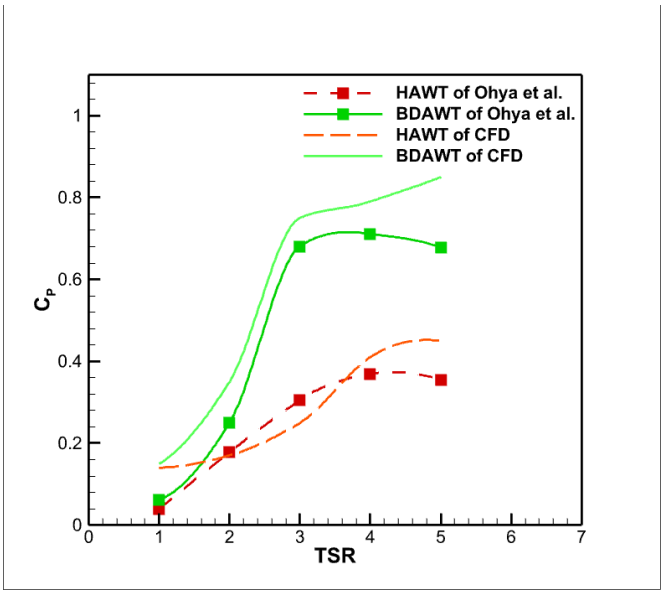

Fig. 5. Comparison of simulated and experimental C_p –TSR curves for HAWT and BDAWT.

3. Numerical solver and Turbulence Modeling

All simulations were performed using a steady-state Reynolds-averaged Navier–Stokes (RANS) solver (ANSYS Fluent). A Multiple Reference Frame (MRF) approach (also known as a "frozen rotor" model) was employed to model the rotating blades in a steady framework: the rotor and its near-field were defined as a rotating sub-domain (rotating at a specified angular velocity ω for each case), while the outer domain remained stationary. This allows the blades' rotation to impart swirl and induction effects on the flow without requiring a time-dependent simulation. The interface between the rotating region and the stationary region was treated with continuity of flow variables, and the solver accounts for the Coriolis and centripetal acceleration terms in the rotating frame.

We solved the incompressible RANS equations with a finite-volume method, using second-order upwind discretization for convection terms and second-order for pressure. Convergence was achieved when residuals fell below 10−5 for continuity and momentum and below 10−6 for turbulence quantities, and when the monitored output forces (torque on the rotor) stabilized.

3.1 Continuity Equation (Mass Conservation)

The continuity equation is a statement of the conservation of mass and ensures that the mass flux in the system is conserved. For incompressible flow, the continuity equation is expressed as

$$\nabla \cdot (\rho u) = 0 \qquad (1)$$

Where:

ρ is the fluid density (here, air), and u is the velocity vector of the fluid.

This equation ensures that the mass of the fluid entering and exiting any control volume remains constant. In CFD simulations of wind turbines, it is used to guarantee that the flow remains steady and that there are no artificial mass accumulations or losses in the domain.

3.2 Navier-Stokes Equations

The Navier-Stokes equations describe the motion of a viscous fluid. They are derived from the principles of conservation of mass, momentum, and energy. For incompressible flow, the Navier-Stokes equations are given by:

$$\partial u/\partial t + u \cdot \nabla u = -(1/\rho)\,\nabla p + \nu\,\nabla^2 u + f \qquad (2)$$

Where:

u is the velocity vector of the fluid, ρ is the fluid density, p is the static pressure, ν is the kinematic viscosity of the fluid, f represents external forces such as the forces exerted by the rotor blades of the wind turbine.

These equations describe how the velocity and pressure fields evolve over time and space due to internal and external forces. Solving the Navier-Stokes equations provides the flow field around the turbine rotor and helps predict phenomena like wake formation, vortex shedding, and pressure distribution.

3.3 Turbulence Modeling: $k-\omega$ Model

In wind turbine simulations, the flow around the turbine blades is typically turbulent. The Reynolds Averaged Navier Stokes (RANS) equations are used to model turbulence. The k-ω model is one of the most widely used two-equation turbulence models that provides an effective way to simulate turbulent flows.

The k-ω model includes two transport equations:

Energy Equation for Turbulence (k):

$$\partial k/\partial t + u \cdot \nabla k = \nabla \cdot [\,(\mu + \sigma_k\,\mu_t)\,\nabla k\,] + P_k - \varepsilon_k \qquad (3)$$

Where:

k is the turbulence kinetic energy, P_k is the production of turbulence kinetic

energy, ε_k is the dissipation of turbulence energy, μ_t is the turbulent viscosity, which is modeled as $\mu_t = \rho\, C_\mu\, k^2/\varepsilon$, σ_k is the turbulent Prandtl number for k.

Turbulence Frequency Equation (ω):

$$\partial\omega/\partial t + u \cdot \nabla\omega = \nabla \cdot [(\mu + \sigma_\omega\, \mu_t)\, \nabla\omega] + (\beta_\omega\, \omega / k)\, P_k - \alpha_\omega\, \omega^2 \quad (4)$$

Where:

ω is the turbulence frequency, P_k is the turbulence production, α_ω and β_ω are constants that control the dissipation and production rates, σ_ω is another constant for the diffusion term of turbulence frequency.

These two equations work together to model the turbulent fluctuations in the flow field around the rotor and provide insights into the turbulence intensity and the behavior of the flow, especially in regions near the rotor blades [25-27]. The incompressible Reynolds-averaged Navier-Stokes (RANS) equations, together with the $SST\ k-\omega$ turbulence model, are presented in their standard form to clearly define the numerical framework and underlying assumptions. Although no modifications are applied to these equations, their inclusion is intended to ensure transparency and completeness of the solution methodology. Detailed theoretical derivations can be found in standard CFD and wind energy textbooks.

3.4 Definition of Tip-Speed Ratio and Test Matrix

The tip-speed ratio (TSR) is defined as the ratio of the linear speed of a blade tip to the free-stream wind speed. In formula form:

$$TSR = \frac{blade\ tip\ speed}{wind\ speed} = \frac{\omega R}{U_\infty} \quad (5)$$

where ω is the rotor's angular velocity (rad/s), R is the rotor radius, and U_∞ is the free-stream wind speed. TSR is a fundamental non-dimensional parameter in wind turbine design because it links the rotation speed with the wind speed. For a conventional three-bladed HAWT, the optimal TSR is typically around 7, meaning the blade tips move roughly 7 times faster than the wind [23]. If TSR is too low, the blades experience a high angle of attack and may stall; if TSR is too high, the blades outrun the wind, operating at low angles of attack with high drag. Most modern turbines, therefore, have a design TSR around 6–8 for peak efficiency.

In our simulations, we examine discrete TSR values of 4, 5, 6, 7, 8, 9, and 10 for both the HAWT and BDAWT. For each TSR value, the rotor's rotational speed ω was set appropriately (for a fixed wind speed U_∞) to achieve the desired TSR. The wind speed was held constant for all cases, so varying TSR effectively means varying the rotor RPM. This approach isolates the effect of rotation speed on performance and flow, allowing a direct comparison between the HAWT and BDAWT under identical wind conditions.

After obtaining converged solutions for each case, we extracted a range of flow data for post-processing: (i) overall performance metrics like the turbine's power output and C_P; (ii) static pressure fields and contours; (iii) velocity fields and streamlines; and (iv) one-dimensional profiles of axial velocity along specified lines in the flow (described next). These analyses illuminate how the diffuser and brim alter the flow and performance relative to the HAWT.

4. Results and Discussion

4.1 Flow Field Characteristics and Velocity Profiles

We first examine the qualitative flow structure around the turbines. Fig. 6 shows path lines (streamlines) colored by turbulent eddy viscosity for both the HAWT and BDAWT across TSR = 4–10. In the BDAWT cases, a clear flow separation and vortex shedding occur immediately downstream of the diffuser's brim, leading to a localized spike in eddy viscosity in that region. This separated circular shear layer (vortex ring) creates a low-pressure region just outside the diffuser exit, which in turn accelerates the core flow through the diffuser outlet by entraining additional air from the surroundings. This vortex-induced suction at the exit enhances mass flow through the rotor and thereby increases energy extraction. By contrast, the HAWT (without a shroud) exhibits only minor changes in eddy viscosity directly downstream of the rotor. Its wake is broader and less focused, with tip vortices dissipating more irregularly into the freestream. As TSR increases toward ~7, the HAWT's wake "depth" (velocity deficit) grows, reflecting maximal momentum extraction by the blades, then diminishes beyond $TSR \approx 7$ due to the onset of blade stall and subsequent wake recovery as rotation induced lift decreases. In the BDAWT, however, the diffuser's pre-acceleration effect and strong static pressure drop produce a consistently narrower, more concentrated wake across the TSR range. Both configurations show wake intensification up to TSR $\approx 6-8$, followed by gradual recovery as turbulence and mixing increase at the higher TSRs [29,30]. Overall, these streamline visualizations qualitatively confirm that the brimmed diffuser introduces organized vortical structures that promote sustained low pressure behind the rotor, as opposed to the more diffuse wake of the conventional HAWT.

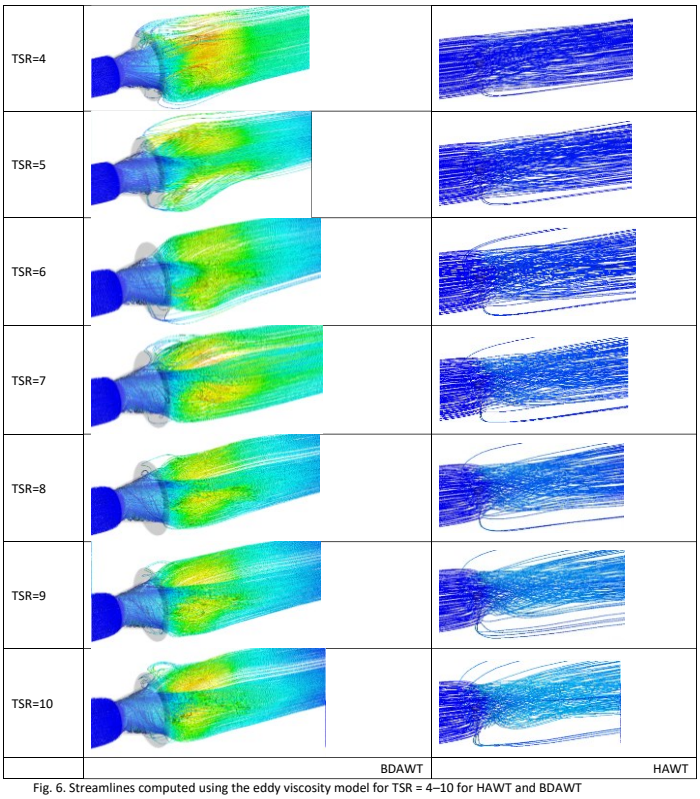

Fig. 6. Streamlines computed using the eddy viscosity model for TSR = 4–10 for HAWT and BDAWT

Turning to the pressure field, Fig. 7 provides contours of static pressure difference (relative to ambient) on representative vertical and horizontal planes cutting through the rotor for both HAWT and BDAWT. In all cases, a negative pressure region (suction) forms in the wake downstream of the rotor. With the diffuser present, this low-pressure wake region is both wider and more intense compared to the HAWT. The diffuser effectively isolates the core flow from outside ambient pressure, and the flow separation at the brim generates intense vortices that induce a sharp pressure drop just downstream of the diffuser's throat. Consequently, the pressure gradient across the rotor (difference between the high pressure on the upstream face and low pressure in the near wake) is increased by the diffuser, which accelerates the flow through the rotor disc (a higher pressure drop drives a higher mass flow). In the HAWT, by contrast, blade-induced flow separations produce more irregular, turbulent vortices that broaden the wake and increase drag, reducing overall efficiency. The BDAWT's controlled vortex shedding behind the brim yields a narrower, more uniform low-pressure wake with stronger suction, thereby enhancing mass flow entrainment and more effectively "pulling" the wind through the turbine. As TSR rises from 4 to around 6–8, both configurations deepen their negative pressure wake (indicating peak momentum extraction around the optimal operating point). Beyond $TSR \approx 8$; however, partial blade stall and boundary layer separation on the blades begin to reduce lift, permitting a gradual pressure recovery and wake contraction in both cases (more pronounced in the HAWT).

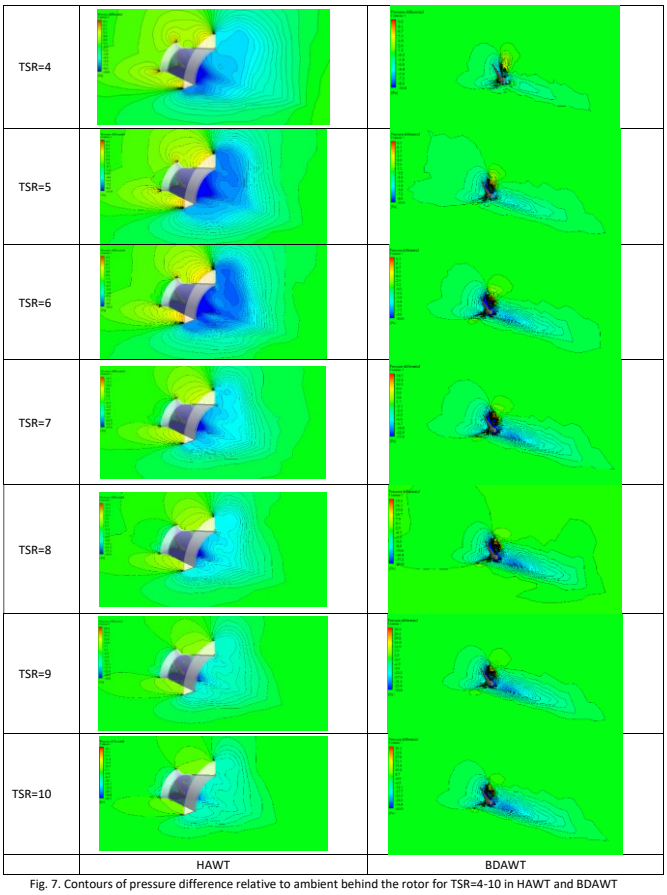

Fig. 7. Contours of pressure difference relative to ambient behind the rotor for TSR=4-10 in HAWT and BDAWT

To quantitatively analyze the velocity field, we defined four measurement lines in the flow (Fig. 8) and extracted time-averaged axial velocity profiles along them for all cases:

Line 1: a vertical line at the diffuser outlet plane (passing through the center of the diffuser exit, aligned with the vertical (Z) axis),

Line 2: a vertical line at the diffuser inlet plane (upstream of the rotor, also along the Z-axis through the rotor centerline),

Line 3: the centerline of the turbine (coinciding with the rotor axis, along the X-axis of the domain),

Line 4: a horizontal line across the diffuser outlet plane (along the Y-axis through the center of the outlet).

These lines are chosen to capture the flow acceleration and deceleration in regions of interest: Line 2 gauges the flow just upstream of the rotor (inflow region), Line 1 and Line 4 characterize the distribution of velocity at the diffuser's exit (the vertical and horizontal cross-sections of the emerging jet/wake), and Line 3 shows how the axial velocity develops from upstream, through the rotor, and out of the diffuser along the centerline.

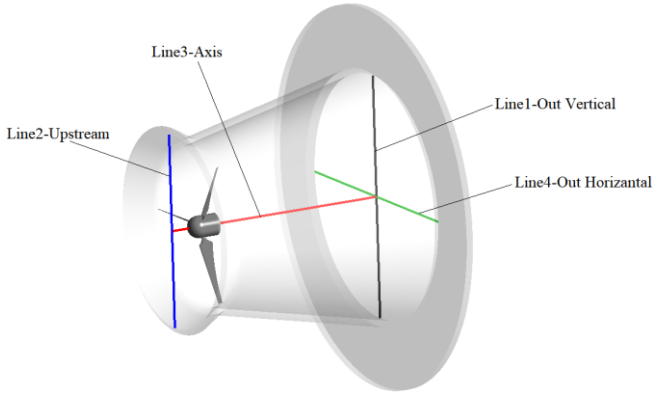

Fig. 8. Reference lines for velocity profile analysis in the wind turbine: Line 1 (black), Line 2 (blue), Line 3 (red), and Line 4 (green).

Fig. 9 presents the axial velocity magnitude profiles along Line 2 (upstream of the rotor, at the inlet plane of the diffuser for BDAWT or an equivalent plane for HAWT) for TSR = 4–10. As TSR increases, the mean velocity along this line rises in both configurations due to stronger drawing of flow into the rotor plane at higher rotational speeds (greater induction effect). The BDAWT, however, shows progressively larger velocity gains relative to the HAWT as TSR grows. This demonstrates that the diffuser's "pumping" effect becomes more pronounced at higher rotor speeds: the faster spinning rotor (with the diffuser) creates a more substantial low-pressure region in the diffuser throat, sucking in the flow ahead of it. In every case, the BDAWT exhibits higher core (centerline) velocities upstream of the rotor compared to the HAWT, reflecting the stronger downstream pressure drop (suction) induced by the shroud. Near the walls of the diffuser (in the BDAWT profiles), a pronounced velocity deficit is observed; this is caused by the boundary layer that develops along the inner diffuser wall, which slows the flow near the surface as it approaches the rotor plane. Additionally, both the HAWT and BDAWT profiles show a slight dip in velocity at the hub height (center of the rotor), an artifact of the rotor hub blocking the flow and causing local deceleration upstream of the rotor center.

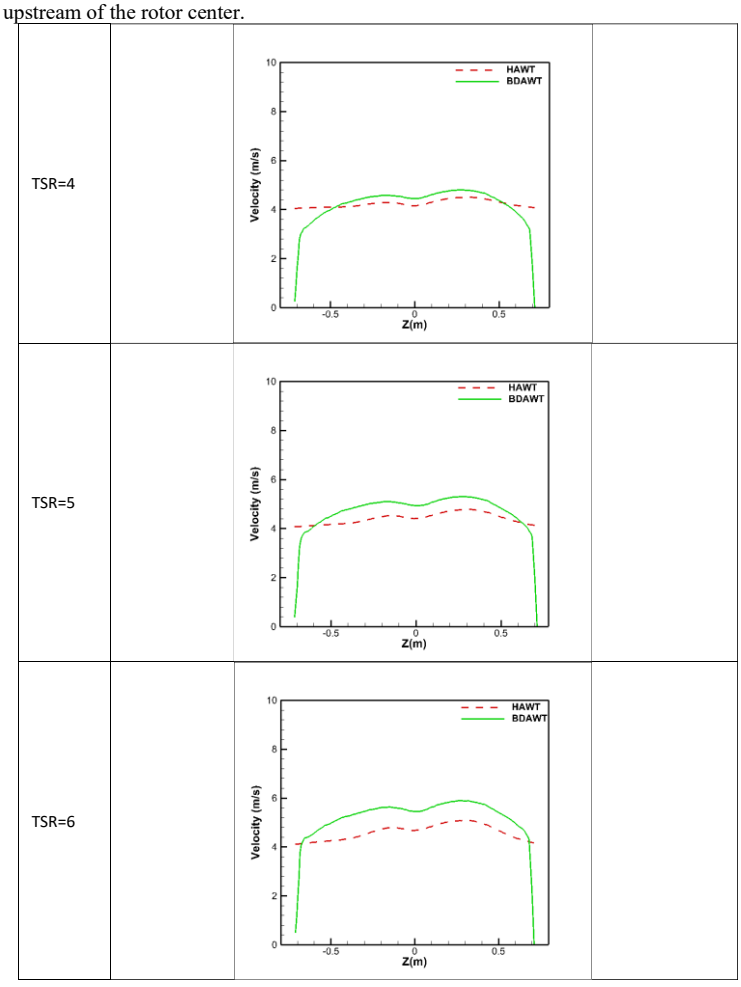

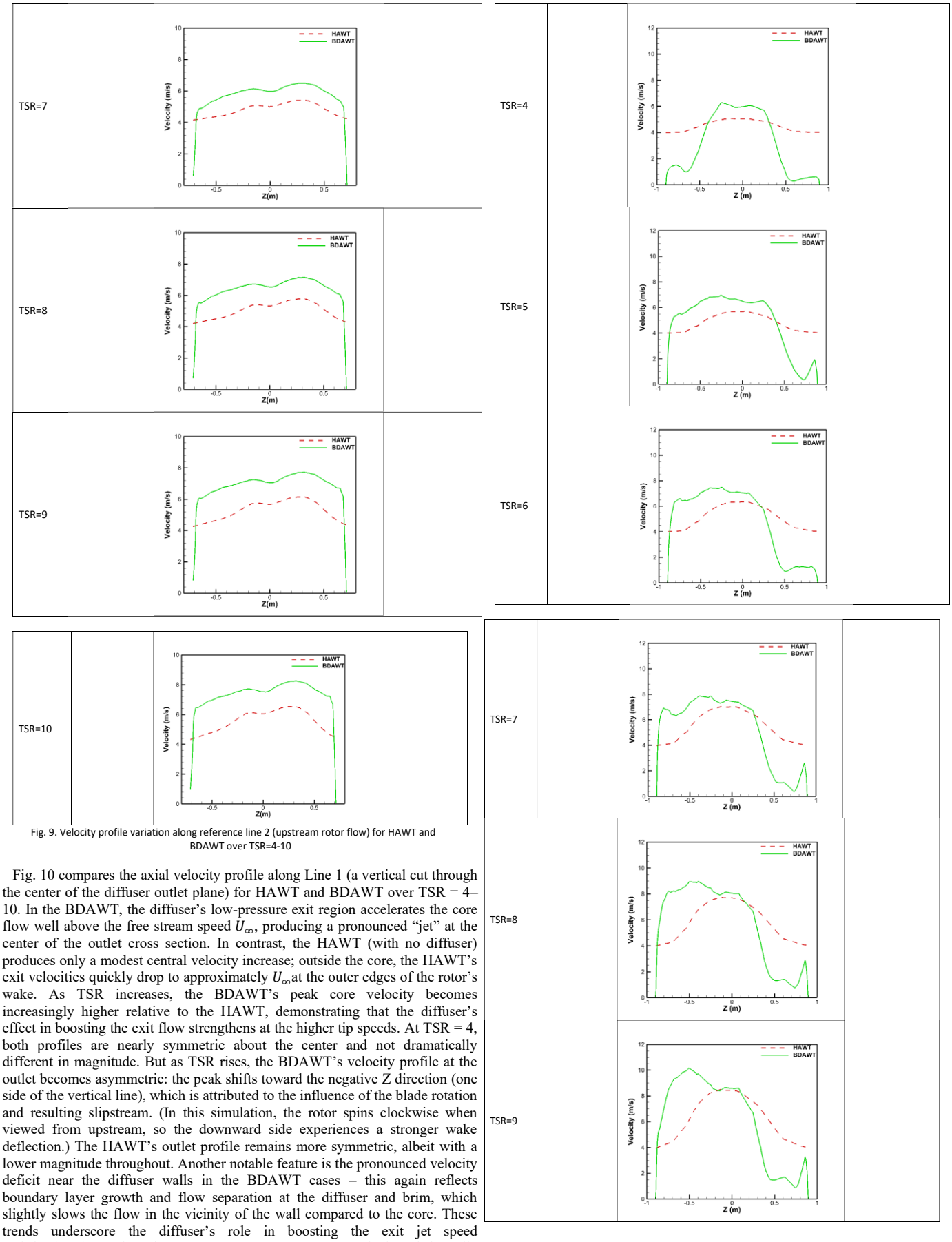

Fig. 9. Velocity profile variation along reference line 2 (upstream rotor flow) for HAWT and BDAWT over TSR=4-10

Fig. 10 compares the axial velocity profile along Line 1 (a vertical cut through the center of the diffuser outlet plane) for HAWT and BDAWT over TSR = 4–10. In the BDAWT, the diffuser's low-pressure exit region accelerates the core flow well above the free stream speed U_∞, producing a pronounced "jet" at the center of the outlet cross section. In contrast, the HAWT (with no diffuser) produces only a modest central velocity increase; outside the core, the HAWT's exit velocities quickly drop to approximately U_∞at the outer edges of the rotor's wake. As TSR increases, the BDAWT's peak core velocity becomes increasingly higher relative to the HAWT, demonstrating that the diffuser's effect in boosting the exit flow strengthens at the higher tip speeds. At TSR = 4, both profiles are nearly symmetric about the center and not dramatically different in magnitude. But as TSR rises, the BDAWT's velocity profile at the outlet becomes asymmetric: the peak shifts toward the negative Z direction (one side of the vertical line), which is attributed to the influence of the blade rotation and resulting slipstream. (In this simulation, the rotor spins clockwise when viewed from upstream, so the downward side experiences a stronger wake deflection.) The HAWT's outlet profile remains more symmetric, albeit with a lower magnitude throughout. Another notable feature is the pronounced velocity deficit near the diffuser walls in the BDAWT cases – this again reflects boundary layer growth and flow separation at the diffuser and brim, which slightly slows the flow in the vicinity of the wall compared to the core. These trends underscore the diffuser's role in boosting the exit jet speed and shaping the wake: the BDAWT creates a more peaked and laterally confined high velocity jet, whereas the HAWT's wake is broader and the velocity tapers to freestream at the edges.

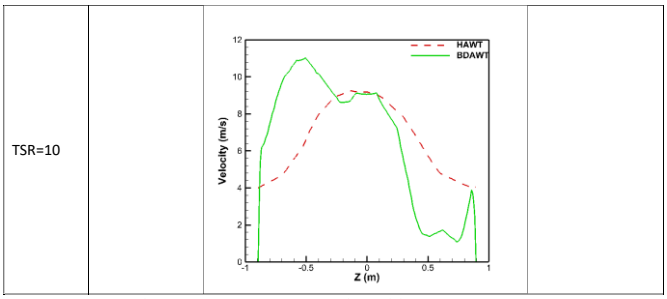

Fig. 10. Velocity profile on the vertical outlet plane (Line 1) for HAWT and BDAWT over TSR = 4–10.

In Fig. 11, the axial velocity profile along Line 4 (a horizontal line through the diffuser outlet) is plotted for both configurations across the TSR range. Similar to the vertical cut, the diffuser case shows a pronounced asymmetry in the horizontal profile at higher TSRs. A local secondary peak in velocity appears adjacent to one side (the negative-Y side) of the outlet in the BDAWT, which is driven by the rotational slipstream and entrainment of high-speed flow by the rotating blades. Essentially, the swirling flow and induced velocity field cause one side of the diffuser outlet to have a slightly higher velocity than the other. The HAWT's horizontal profile, by comparison, is more uniform and symmetric, lacking such secondary peaks. Moreover, with increasing TSR, the BDAWT's high-speed core velocity (at the center of the outlet) decreases slightly for the highest speeds, and by TSR = 10 the central outlet velocities in the BDAWT case almost match those of the HAWT. This indicates that at very high tip-speed ratios, the advantage conferred by the diffuser on the absolute exit velocity diminishes. This is likely because at extremely high rotor speeds, the flow inside the diffuser becomes more turbulent and possibly partially separated, which limits further acceleration, effectively, the rotor's own inefficiencies (stall, drag) start to dominate, and the diffuser's benefit saturates.

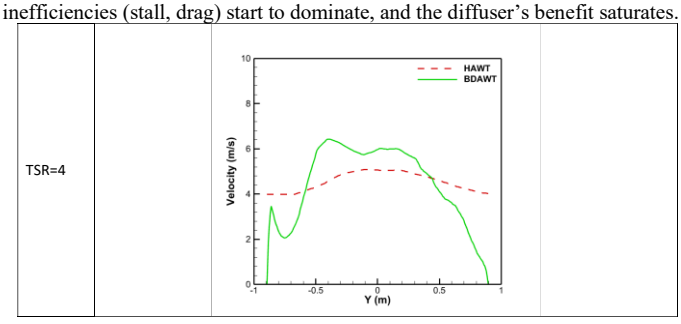

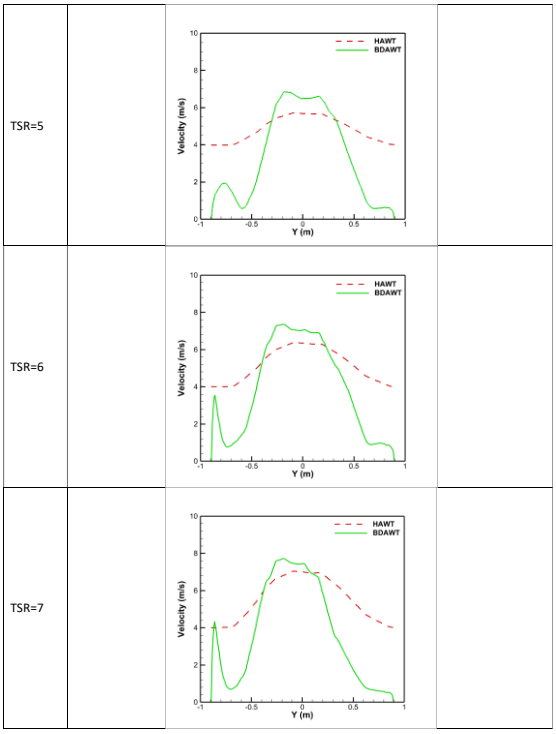

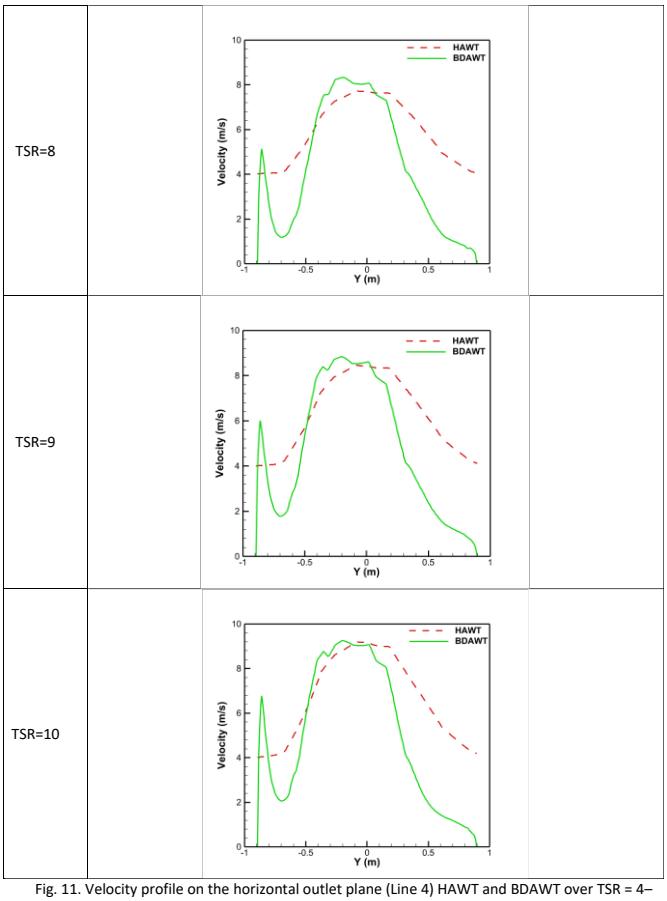

Fig. 11. Velocity profile on the horizontal outlet plane (Line 4) HAWT and BDAWT over TSR = 4–10.

Finally, Fig. 12 plots the axial velocity along Line 3 (the central axis of the turbine) from a point upstream of the rotor (at $x \approx -0.5\ m$, in the free stream) through the rotor plane (x = 0) and down to the diffuser outlet (approximately $x \approx 1.5\ m$ for the BDAWT). This gives a longitudinal cut of how the axial velocity changes through the turbine for both HAWT and BDAWT across the TSR range. Upstream of the blades (moving along the $-x$ direction toward the rotor), the flow in both cases decelerates from U_∞ down to the blade inflow speed due to the induction effect of the rotor (air is slowed as it approaches the rotor, piling up slightly). At x = 0 (the rotor plane), the velocity has its minimum. Immediately downstream of the rotor (just past x = 0), there is a further dip for both configurations, this is because the rotor extracts energy and imposes a sudden pressure drop, causing the flow to slow further in the near wake. After this point, the behavior diverges: in the BDAWT, the diffuser's converging section and strong suction drive a pronounced acceleration of the flow along the axis, reaching a peak velocity around $x \approx 1.0\ m$ (which is inside the diffuser, before the exit plane). This peak axial velocity in the BDAWT's core flow exceeds the HAWT's centerline velocity at the same location. Beyond this peak, in both configurations, the axial velocity gradually decays toward the far-outlet value (which will approach U_∞ again further downstream). Notably, at TSR = 4, the BDAWT maintains significantly higher centerline velocities than the HAWT throughout the diffuser, but as TSR increases to 10, the two profiles converge, indicating that the diffuser's relative acceleration effect diminishes at very high TSRs (as seen earlier, likely due to increased losses at high rotation speeds). In summary, the centerline data reaffirm that the diffuser strongly boosts the near wake velocity (and thus mass flow) at moderate TSRs, but this boost is somewhat reduced at the extreme high end of the tested TSR range.

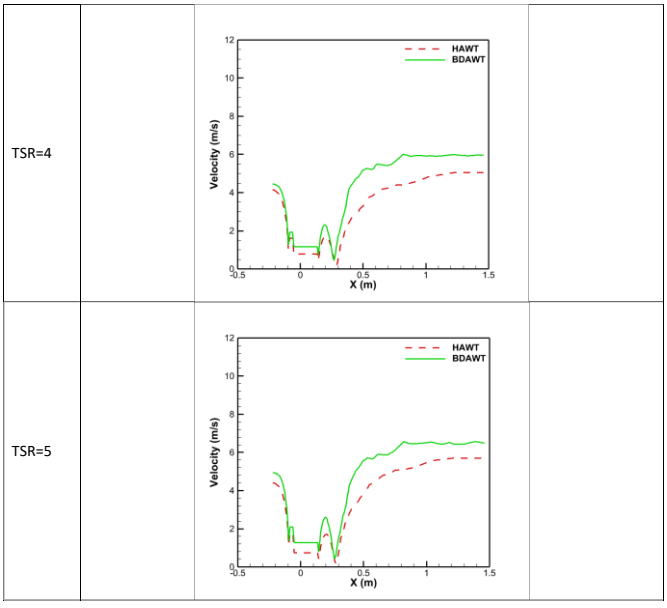

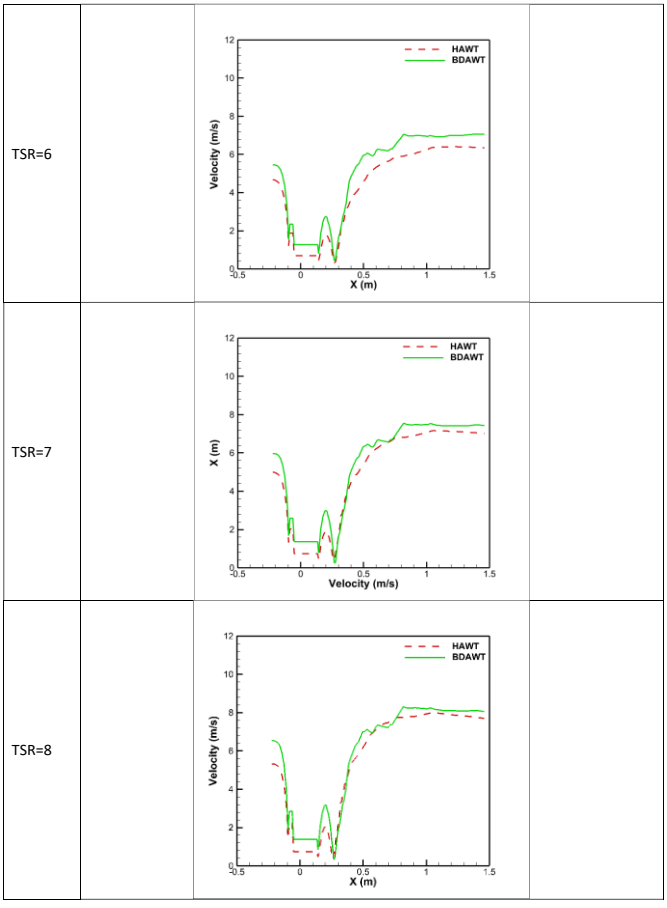

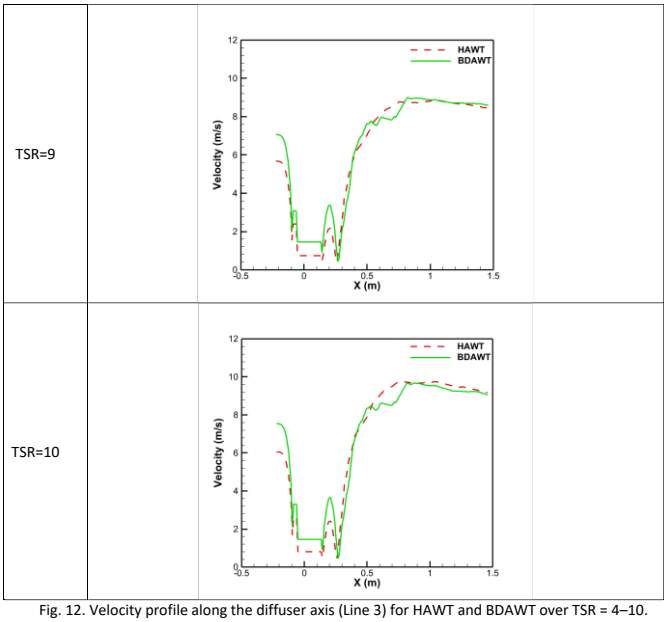

Fig. 12. Velocity profile along the diffuser axis (Line 3) for HAWT and BDAWT over TSR = 4–10.

4.2 Performance Metrics: Power Coefficient and Induction

The power coefficient C_P of a wind turbine is defined as the fraction of the wind's kinetic power (through the rotor's swept area) that the turbine extracts as mechanical power. In formula form:

$$C_P = \frac{P_{turbine}}{P_{wind}} = \frac{P_{turbine}}{½ \cdot \rho \cdot A \cdot U_\infty{}^3} \quad (6)$$

where $P_{turbine}$ is the turbine's output power, A = πR² is the rotor swept area, ρ is air density, and "U_∞" is the free-stream wind speed. Essentially, C_P measures the fraction of available wind energy that is converted into useful mechanical energy. A higher C_P indicates more efficient extraction of energy. Conventional three-blade HAWTs are fundamentally limited by Betz's law to a maximum ideal C_P of 0.593 (59.3%). In practice, modern large HAWTs peak around 75–80% of the Betz limit (i.e., $C_P \approx 0.44 - 0.48$ under optimal conditions) [2,5,25]. Losses due to tip vortices, nonuniform flow, airfoil drag, etc., prevent them from reaching the ideal.

A BDAWT, however, can augment the wind stream through the rotor by lowering the pressure at the exit and streamlining the expansion of the flow. This effectively draws a larger mass flow through the blades than what the rotor's area alone would intercept, allowing the turbine to exceed the Betz limit when C_P is referenced to the rotor's area alone (because additional kinetic energy from outside the rotor's swept area is pulled in). In other words, the effective wind power intercepted is larger than $½ \cdot \rho \cdot A \cdot U_\infty{}^3$. Experiments and simulations have indeed shown diffuser augmented turbines reaching significantly higher power coefficients than conventional rotors [3,26,28]. Throughout this study, the power coefficient is defined as $Cp = \frac{P}{1/2\rho A U_\infty^3}$, where $A = \pi R^2$ is the rotor swept area and U_∞ is the free-stream velocity, for both the HAWT and the diffuser augmented turbine. With this definition, C_p values exceeding the Betz Joukowski limit may occur for the BDAWT due to diffuser-induced mass flow augmentation. Such values do not violate momentum theory, as the diffuser enlarges the effective flow stream tube feeding the rotor and modifies the underlying assumptions of the classical Betz analysis.

Fig. 13 compares the variation of the power coefficient C_P with TSR for the HAWT and BDAWT configurations. Across the entire TSR range (4–10), C_P is consistently higher for the BDAWT. At TSR = 4, the HAWT's C_P is quite low (since at low tip speeds the rotor is operating far below its optimal lift conditions), while the BDAWT already shows a substantial improvement due to the diffuser's ability to channel more flow through the rotor even at this suboptimal rotor speed. As TSR increases, both turbines' C_P values rise to a peak and then decline, but the BDAWT's curve lies above the HAWT's at all points. The HAWT reaches a maximum C_P of about 0.39 at $TSR \approx 7$, after which C_P slightly decreases at $TSR\ 8 - 10$ (a sign of diminishing returns and onset of aerodynamic losses as the blades start operating at less favorable angles of attack or minor stall). In contrast, the BDAWT's C_P continues increasing up to TSR ≈ 8, reaching a maximum around 0.59 (approximately 51% higher than the HAWT's peak). Beyond TSR 8, the BDAWT's C_P also experiences a slight drop-off by TSR 10. The reason for the BDAWT's decline at very high TSRs is that excessive rotational speed can induce local flow separation inside the diffuser (particularly along the diffuser's divergent section), as well as increased viscous losses, which together reduce the marginal gains in power and can even slightly reduce the mass flow enhancement. Nonetheless, the BDAWT maintains a notably higher C_P across a broad range of

TSRs, indicating a more forgiving and extended high-efficiency operating window.

Two mechanisms primarily drive the BDAWT's superior power capture: (1) The diffuser (especially with the brim) induces a strong static pressure drop at its exit, effectively sucking more air through the rotor disc (increasing mass flow and available energy); (2) The diffuser's shape allows the flow to expand and recover pressure more gradually after the rotor, maintaining a lower pressure in the rotor plane and sustaining a larger pressure differential across the rotor. In essence, the rotor in a BDAWT experiences a larger pressure force for a given flow rate, and the flow rate itself is higher, more power is extracted. In a classical HAWT, Betz's law limits C_P to 0.593 (59.3%) at an optimum induction factor (as discussed below), whereas in a BDAWT, when referencing C_P to the rotor area, values of 0.6–0.8 or higher have been reported without violating energy conservation principles (the "excess" energy comes from air that is bypassing a traditional rotor but is captured by the diffuser augmented system).

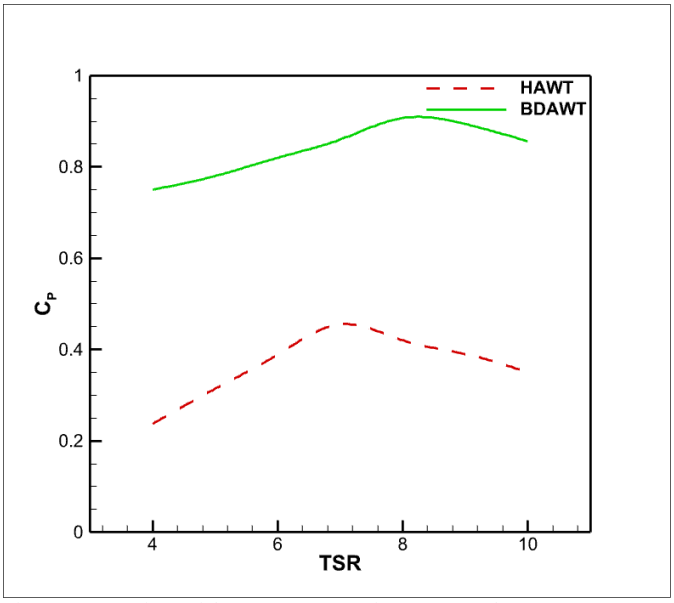

Fig. 13. Comparison of the C_P versus TSR for HAWT and BDAWT

It is informative to interpret these results in terms of the induction factor and the momentum theory. In HAWT aerodynamics, the axial induction factor "a" is defined as the fractional reduction in wind speed between the free-stream and the rotor plane:

$$a = \frac{U_\infty - U_{rot}}{U_\infty} = 1 - \frac{U_{rot}}{U_\infty} \quad (7)$$

where U_{rot} is the wind velocity at the rotor plane (downstream of the induction zone) and U_∞ is the undisturbed free stream wind speed. If the rotor slows the flow significantly, a is large (approaching 0.5 in the extreme case of a heavily loaded rotor). From one-dimensional momentum theory, this slowdown corresponds to a static pressure drop across the rotor disc, which produces a thrust force on the rotor and extracts kinetic energy from the flow, manifesting as a reduced downstream velocity (a wake deficit). Physically, increasing a (stronger induction) draws more mass flow through the rotor – enhancing the pressure differential upwind and downwind and boosting energy extraction – but also deepens the wake and can promote blade flow separation and vortex shedding if a exceeds about 0.3–0.5. Betz's theory gives the well-known relation between a and the ideal power coefficient:

$$C_P = 4a(1-a)^2 \quad (8)$$

which predicts a theoretical maximum $C_P = 16\!/\!27 \approx 0.593$ at a = 1/3 (where the wind velocity at the rotor plane is 2/3 of the free stream, and the far wake velocity is 1/3 of free-stream). In practice, modern HAWTs operate at an a around 0.2–0.3 (yielding $C_P \approx 0.4 - 0.5$) to optimize lift-to-drag performance and avoid excessive wake losses or stall. Turbines use pitch control and adjust TSR to maintain a near its optimal value under varying wind conditions. When a approaches 0.5, the downstream wake velocity becomes very low (almost stagnating), and the simple momentum theory breaks down (requiring more advanced models to account for wake expansion and turbulence). Thus, the interplay between induction (a), pressure drop, and flow stability governs turbine design and operation: maximizing energy capture while preventing excessive aerodynamic loading.

In a BDAWT, the concept of induction can be extended: since the flow continues to accelerate within the diffuser, one can measure the wake velocity at the diffuser exit rather than at the rotor plane. We can define a generalized induction factor $\bar{a}$ for the diffuser-augmented flow as:

$$\bar{a} = 1 - \frac{U_{diff}}{U_\infty} \quad (9)$$

Where " U_{diff} " is the wind speed at the diffuser exit. Because the diffuser and brim lower the static pressure at the outlet and generate vortices that pre-accelerate the flow through the rotor, the exit velocity U_{diff} in a BDAWT can actually be greater than the free stream velocity U_∞ (i.e., the core flow is accelerated above the ambient wind speed). In such cases, μ > 1 ($\frac{U_{diff}}{U_\infty} = \mu$), leading to a negative value of $\bar{a}$ if one used the above formula directly. This indicates that the simple definition of a needs reinterpretation for a shrouded turbine, essentially, the diffuser causes a pre-acceleration rather than a pure deceleration through the rotor plane. We can still utilize the momentum disk concept by considering how the diffuser augments the mass flow. In a BDAWT, a more useful parameter is the velocity ratio at the diffuser exit, defined as $\mu = \frac{U_{diff}}{U_\infty}$. Typically for a well-designed diffuser, μ > 1 (e.g., 1.1–1.2 or higher), whereas for a stand-alone HAWT, the velocity in the far wake is lower than free-stream (approximately (1 – 2a) U_∞, which at optimum a = 1/3 yields 1/3 U_∞). In summary, the diffuser's presence means the flow does not slow down as much (or at all) in the far wake; instead, it may speed up, so the "induction factor" concept adapts: the BDAWT effectively has a negative wake induction (in the sense of acceleration). A larger μ (>1) corresponds to a stronger diffuser-induced suction and thrust.

According to Betz's law, the optimal balance between energy capture and wake kinetic energy loss for a bare rotor occurs at a velocity ratio μ (rotor plane) of 1/3 (with a = 1/3). For the BDAWT, since μ (diffuser exit) > 1, the classical Betz limit no longer directly applies to the rotor alone area. Instead, one can derive a diffuser augmented power coefficient that accounts for the combined effect of rotor induction and diffuser augmentation. One simple theoretical approach (proposed by Watanabe & Ohya [31]) is to express the BDAWT power coefficient as the product of two factors: the classical Betz rotor performance (dependent on a) and the diffuser's velocity augmentation factor μ. In essence:

$$C_{P-BDAWT} \approx \mu.[4\bar{a}(1-\bar{a})^2] \quad (10)$$

where a might be taken as the rotor's own induction factor and $\mu = \frac{U_{diff}}{U_\infty}$ is the diffuser's velocity ratio. Because the diffuser can make μ > 1, the BDAWT's peak CP (at its optimal combination of $\bar{a}$ and μ) can exceed the HAWT's peak. In our CFD results, the BDAWT achieved a maximum CP ≈ 0.59 (with μ around 1.1 and an effective induction higher than the HAWT's), whereas the HAWT peaked at CP ≈ 0.39.

To illustrate these theoretical considerations, Fig. 14 plots the axial induction factor a (based on rotor plane velocity for HAWT and diffuser exit velocity for BDAWT) and the ideal Betz power coefficient ($4a(1-a)^2$) as functions of TSR, for both configurations. For the HAWT, the induction factor "a" increases steadily with TSR up to ~7, reaching a maximum of $a \approx 0.128$ (12.8%). This relatively low induction at peak power (compared to the Betz-optimal 33%) is typical for a real turbine, since blade aerodynamic efficiency is optimized at a lower induction to avoid stall. Beyond TSR 7, a for the HAWT declines as TSR increases further, due to the reduced angle of attack and eventual stall, this aligns with the earlier observation that CP drops after 7. The corresponding Betz limit CP Betz curve for the HAWT (using the instantaneous a) rises to ~0.40 at TSR 7 and then falls, roughly mirroring the actual CP behavior (peak 0.39 at TSR 7). In contrast, for the BDAWT, the "effective" induction factor $\bar{a}$ (based on diffuser exit velocity) starts at a modest value for low TSR and rises more gradually, reaching approximately $\bar{a}$= 0.345 (34.5%) at TSR = 10. This suggests that the BDAWT operates at a much higher overall induction by the time TSR = 10, thanks to the diffuser, it is drawing significantly more flow (in a momentum theory sense) than the HAWT. Physically, the BDAWT's low-pressure wake and brim induced vortices sustain stronger suction, pulling additional mass flow through the rotor and delaying flow separation even at high TSRs. The ideal Betz CP corresponding to the BDAWT's $\bar{a}$ reaches about 0.59 (when $\bar{a}$≈ 0.33–0.34, near optimal) and stays around 0.57–0.59 for $\bar{a}$ up to 0.345. Notably, the actual BDAWT's CP in our CFD (the red curve in Fig. 14) is close to 0.59 at TSR 7–9, which matches the theoretical Betz prediction at those effective induction values, except that this 0.59 is achieved at a much higher mass flow (with μ > 1) than the HAWT could manage. In fact, the BDAWT's CP remains high (~0.55 – 0.59) from TSR 7 through 9 (a plateau of near optimal performance), whereas the HAWT has a sharp peak at 7 and then declines. By TSR 10, the BDAWT's CP has only slightly decreased (to ~0.56 – 0.57), whereas the HAWT's dropped to ~0.34. This plateau in BDAWT performance arises because the diffuser augmentation maintains high core velocities and a sustained pressure drop across the rotor; even as the blades start to generate more drag at very high speeds, the additional flow pulled by the diffuser compensates, so power extraction does not diminish as quickly with increasing TSR.

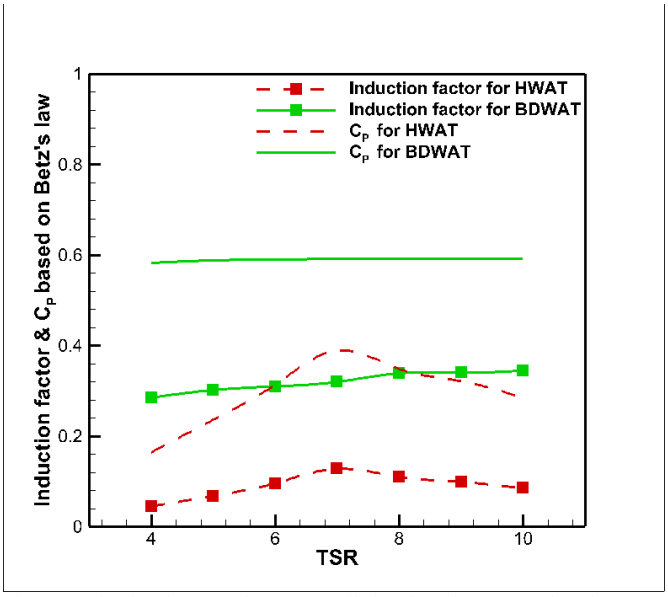

Fig. 14. Induction factor and power coefficient based on Betz's law for HAWT and BDAWT over TSR =4–10

To further quantify the rotor flow interaction, the axial induction factor is evaluated using two complementary definitions. The standard rotor plane axial induction factor is defined a $a_{rotor} = 1 - \frac{U_{rotor}}{U_\infty}$, where U_{rotor} is the area averaged axial velocity at the rotor plane. This definition is consistent with classical momentum theory and is directly applicable to the conventional HAWT, which exhibits positive induction corresponding to a velocity deficit at the rotor.

For the diffuser augmented turbine, the diffuser induced pressure field can accelerate the flow through the rotor plane, resulting in $U_{rotor} > U_\infty$ and negative values of a_{rotor}. While physically meaningful, this behavior is more clearly interpreted using a diffuser referenced metric. Therefore, the diffuser-based axial induction factor is also defined as $a_{diff} = 1 - \frac{U_{diff}}{U_\infty}$, where U_{diff} is the axial velocity at the diffuser exit plane. This parameter more directly represents diffuser induced suction and mass flow augmentation. Table 1 compares the axial induction factors for both turbines over the investigated TSR range, highlighting the fundamental difference between the classical velocity deficit behavior of the HAWT and the flow acceleration regime of the diffuser augmented turbine.

Table 1 . Axial Induction Factor vs TSR for HAWT and BDAWT

TSR	a_{rotor} (HAWT)	a_{diff} (BDAWT, diffuser plane)	a_{rotor} (BDAWT, rotor plane)
4	0.04	0.28	-0.20
5	0.06	0.30	-0.21
6	0.09	0.31	-0.22
7	0.13	0.32	-0.23
8	0.11	0.33	-0.25
9	0.10	0.33	-0.15
10	0.09	0.34	-0.05

Another useful metric is the rotor-plane velocity ratio μ, defined (for a traditional turbine) as:

$$\mu = \frac{U_{rot}}{U_\infty} = 1 - a \quad (11)$$

which quantifies what fraction of the free-stream speed remains at the rotor plane after the flow decelerates due to the turbine's induction. According to one-dimensional momentum theory, the wind speed at the rotor plane is $U_{rot} = U_\infty(1 - a)$, and in the far wake it is $U_{wake} = U_\infty(1 - 2a)$. Physically, a lower μ (i.e., a greater drop in velocity at the rotor) implies stronger momentum extraction — a larger pressure drop across the rotor — resulting in increased thrust force and a deeper downstream wake. Betz showed that the optimal compromise between energy capture and wake loss occurs at $a = \frac{1}{3}$, which corresponds to $\mu = \frac{2}{3}$ and yields CP = 16/27 ≈ 0.593 [2,16,29,31].

Fig. 15 plots the rotor plane (or diffuser exit) velocity ratio μ against TSR for both the HAWT and BDAWT. For the HAWT, μ decreases (i.e., rotor plane wind speed decreases relative to free stream) as TSR increases from 4 to 7, reaching a minimum of μ ≈ 0.872 at TSR = 7. This is the point of maximum momentum extraction (highest a ∼0.128) for the HAWT. Beyond TSR 7, μ rises again (to about 0.94 by TSR 10) because the blades can no longer draw as much momentum – their lift has tapered off due to higher rotational speed and less favorable angle of attack, leading to a reduction in induction (a drops, so $\mu = 1 - a$ increases). In the BDAWT, by contrast, μ (measured at the diffuser exit, which we use as an analog of rotor plane for the augmented case) starts above 1 at low TSR and then gradually declines across the TSR range, reaching $\mu \approx 1.112$ at TSR = 10. At TSR = 4, the BDAWT's diffuser exit velocity ratio was even higher (approximately 1.2). This continuous decrease in μ for the BDAWT indicates that as the rotor spins faster, the relative acceleration (μ) provided by the diffuser becomes a bit less extreme, but it remains above 1 even at TSR 10. In simple terms, the diffuser augmented turbine always has an exit flow speed higher than the free stream wind in our tested range, though the margin above free stream is largest at lower TSR and narrows slightly at high TSR. The initial high μ (e.g., ∼1.2) at low TSR reflects that even when the rotor is not extracting much power (low induction), the diffuser's geometry still funnels and accelerates the wind. As the rotor extraction ramps up with higher TSR, it "uses up" more of that available energy, so the exit velocity relative increase isn't as large, though still >1. Additionally, the rate of decline in μ for the BDAWT is steeper up to TSR ≈ 8 and then tapers off by TSR 10. This corresponds to the earlier observation: up to TSR 8, the rotor and diffuser together are increasing induction and momentum extraction; beyond 8, additional TSR mainly adds losses (turbulence, some separation in diffuser), so μ doesn't drop much further. Importantly, across all TSR values, the BDAWT's velocity ratio (measured at diffuser exit and inlet) remains higher than the HAWT's rotor plane velocity ratio. This confirms that the BDAWT consistently maintains a stronger suction and draws a greater flow through the turbine than the HAWT does.

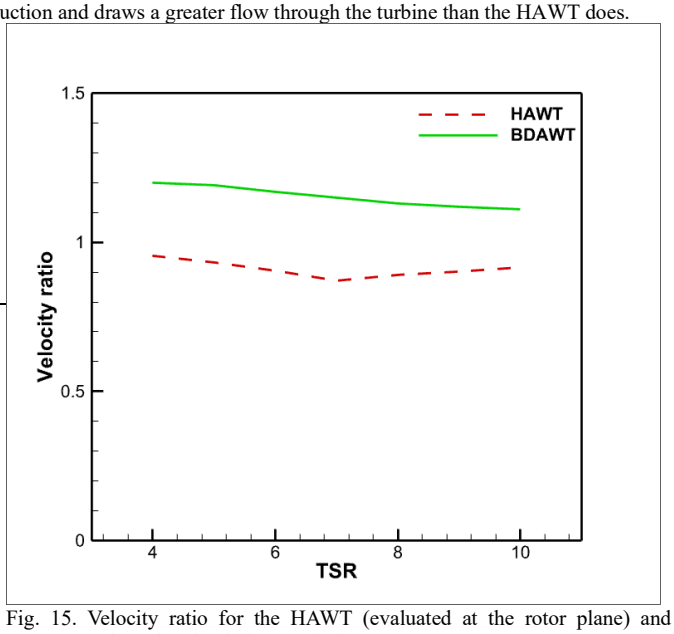

Fig. 15. Velocity ratio for the HAWT (evaluated at the rotor plane) and the BDAWT (evaluated at the diffuser exit plane) over TSR = 4–10.

Because the governing flow mechanisms differ between a conventional HAWT and a diffuser augmented turbine, axial induction and velocity related parameters are evaluated at different reference planes. Rotor plane quantities are used to describe classical rotor induced effects, whereas diffuser plane quantities are introduced to characterize diffuser induced suction and mass flow augmentation. Table 2 summarizes the definitions, reference planes, and physical meanings of the parameters used in this study.

Table 2. Definition and physical interpretation of induction and velocity parameters used for HAWT and BDAWT

Parameter	Symbol	Definition	Reference plane	Applicable turbine	Physical meaning
Axial induction factor (rotor-based)	a_{rotor}	$1 - \frac{U_{rotor}}{U_\infty}$	Rotor plane	HAWT, BDAWT	Quantifies flow deceleration ($a_{rotor} > 0$) or acceleration ($a_{rotor} < 0$) at the rotor due to aerodynamic loading
Axial induction factor (diffuser-based)	a_{diff}	$1 - \frac{U_{exit}}{U_\infty}$	Diffuser exit plane	BDAWT	Represents effective bulk pressure and flow deceleration or acc ass wit diff ind suc
Rotor-plane velocity ratio	μ_{rotor}	$\frac{U_{rotor}}{U_\infty}$	Rotor plane	HAWT	Ir vel def rot con wit mo the
Diffuser exit velocity ratio	μ_{diff}	$\frac{U_{exit}}{U_\infty}$	Diffuser exit plane	BDAWT	M net acc and flo augmentation produced by the diffuser

To more directly quantify the combined effect of the diffuser and rotor on power, we define a diffuser power coefficient C_{P-diff} (sometimes called "augmentated power coefficient") that incorporates both the classical rotor induction effect and the flow pre-acceleration by the diffuser. One way to express this (building on the earlier discussion) is:

$$C_{P-diff} = \mu_{diff} \left[4\, \bar{a}\, (1 - \bar{a})^2 \right] \quad (12)$$

where $\bar{a}$ is an induction factor appropriate for the diffuser augmented case (e.g., based on the flow at the diffuser exit) and $\mu_{diff} = \frac{U_{diff}}{U_\infty}$ is the diffuser's velocity augmentation. In this formulation, the term in square brackets is essentially the Betz–Joukowski function for power extraction from the slowed core flow, and the leading factor μ accounts for the fact that the core flow itself is faster (i.e., more mass flow and energy available) due to the diffuser. Physically, the Betz function $4a(1-a)^2$ describes how the power extracted from a decelerated flow increases with induction up to an optimum (a = 1/3) and then declines if the flow is slowed too much (due to wake losses) [2,28]. The factor μ (>1 for a diffuser) captures the diffuser's contribution by effectively multiplying the available energy flux. Together, these effects allow C_{P-diff} to surpass the classical Betz limit and significantly improve the overall efficiency of a diffuser augmented turbine [31].

Fig. 16 shows the computed diffuser power coefficient (based on our CFD results) as a function of TSR for the BDAWT. Here C_{P-diff} is simply taken as the BDAWT's CP (since we already normalize by rotor area in CP). As shown, C_{P-diff} increases continuously over the entire range TSR 4–10. However, the rate of increase is steeper up to approximately TSR ≈ 6, and then the curve becomes more gradual from TSR 7 onward. The rapid initial rise (from TSR 4 to ~6) reflects the converging–diverging diffuser's strong influence at moderate rotor speeds: during this regime, increasing the rotor speed yields disproportionately large gains in power because the diffuser is effectively amplifying the rotor's induction effect (the flow acceleration and suction are very effective, and the rotor is not yet suffering losses). This is evidenced by the BDAWT's CP surpassing the Betz limit (0.593) already at TSR ≈ 5–6 and then far exceeding it for TSR ≥ 7. Beyond ~6, as TSR continues to increase, the incremental gains in C_{P-diff} taper off. This flattening of the curve beyond TSR ≈ 7–8 arises from the onset of boundary-layer separation in parts of the diffuser's divergent section and heightened turbulence losses at very high flow speeds through the shroud. Essentially, some flow energy is lost to vortices and friction, so the diffuser's augmentation effect does not keep increasing indefinitely with rotor speed. Nevertheless, C_{P-diff} at TSR 10 is the highest of all (around 0.57–0.59, matching the peak near TSR 8–9 within a small margin). Importantly, at all TSR values tested, the BDAWT's power coefficient exceeds the classical Betz CP (16/27 ≈ 0.593) referenced to the rotor area, and the gap between the BDAWT curve and the Betz limit widens as TSR increases. This underlines the effectiveness of the diffuser and brim in enhancing the pressure differentials and mass flow through the rotor, even when the rotor's own efficiency starts to drop off at very high TSR, the system as a whole still outperforms any bare turbine.

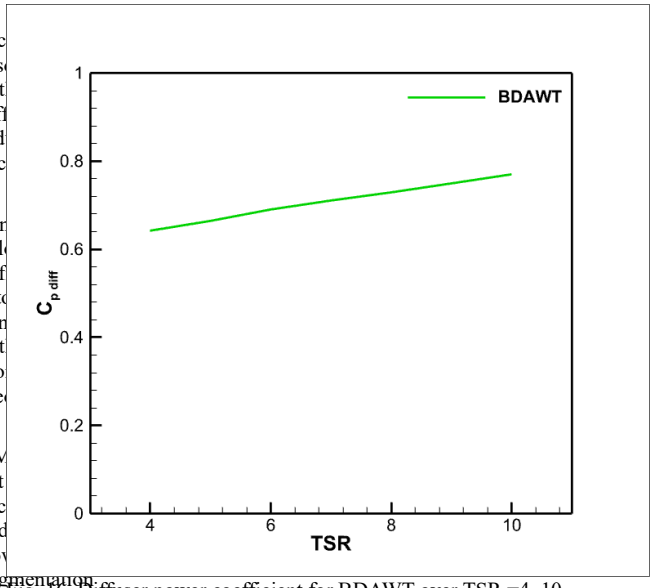

Fig. 16. Diffuser power coefficient for BDAWT over TSR =4–10

Finally, we examine the back-pressure coefficient, which provides another perspective on the pressure-driven flow augmentation. Here, we define C_{bp} as a dimensionless measure of the static pressure difference induced by the turbine (and diffuser) between an upstream station and a downstream station, normalized by the free-stream dynamic pressure. Specifically, one can write:

$$C_{bp} = \frac{P_{upstream} - P_{downstream}}{\frac{1}{2}\,\rho {U_\infty}^2} \quad (13)$$

For a wind turbine in operation, $P_{upstream}$ (just ahead of the rotor) is typically slightly above ambient (due to flow deceleration and pressure buildup), and $P_{downstream}$ (behind the rotor or at the diffuser exit) is below ambient (due to the suction effect). Thus, $(P_{upstream} - P_{downstream})$ is negative for a bare turbine, yielding a negative C_{bp}. A more negative C_{bp} corresponds to a larger pressure drop across the rotor, which usually means stronger induction and thrust. Conversely, if a configuration were to produce a higher pressure at the downstream point than upstream (which is unusual in open flow but could happen locally with a diffuser's vortex), C_{bp} would be positive. In essence, $|C_{bp}|$ indicates the strength of the suction (pressure drop) the turbine generates, and the sign of C_{bp} indicates whether the flow is overall decelerated ($C_{bp} < 0$, as in a normal turbine wake) or somehow accelerated relative to freestream ($C_{bp} > 0$).

Applying Bernoulli's equation between an upstream location (0) in the free stream and a downstream location (1) in the wake (assuming negligible elevation difference and using measured velocities for pressure recovery), we can derive an expression for C_{bp} in terms of the velocity ratio $\mu_{out} = \frac{U_{out}}{U_\infty}$.

Starting from Bernoulli:

$$P_0 + \frac{1}{2}\rho {U_\infty}^2 = P_1 + \frac{1}{2}\rho {U_{out}}^2 \quad (14)$$

(For steady flow along a streamline, neglecting viscous losses). Rearranged for the pressure difference:

$$P_0 - P_1 = \frac{1}{2}\rho({U_{out}}^2 - {U_\infty}^2) \Rightarrow C_{bp} = \frac{P_0 - P_1}{\frac{1}{2}\rho {U_\infty}^2} = \frac{{U_{out}}^2}{{U_\infty}^2} - 1 \quad (15)$$

$$\Rightarrow C_{bp} = {\mu_{out}}^2 - 1 \quad (16)$$

However, in our discussion above we implied C_{bp} is negative for the HAWT (where $\mu < 1$) and positive for the BDAWT (where $\mu > 1$). This discrepancy is because of how we oriented the pressure difference ($P_{upstream} - P_{downstream}$). If instead we consider the magnitude of pressure drop, it might be easier to interpret: a larger $|C_{bp}|$ means a larger pressure differential. For consistency with our CFD results, we treat C_{bp} as a back-pressure coefficient such that a negative C_{bp} denotes the rotor is causing a net pressure drop (suction) relative to ambient (as in a usual turbine wake), and a positive C_{bp} would mean an effective pressure rise or "push" at the rotor (which doesn't happen in these cases except by the diffuser's influence on reference values). Here, the coefficient C_{bp} is defined as a back pressure coefficient representing the normalized pressure difference across the rotor or rotor-diffuser system. A negative value of C_{bp} indicates a net pressure drop (suction) associated with energy extraction, as typically observed in conventional HAWTs. For the diffuser-augmented configuration, the downstream reference pressure is taken at the diffuser exit, where strong flow acceleration and pressure redistribution occur. As a result, the computed C_{bp} may appear positive due to the chosen reference locations, even though the flow is still driven by a net pressure drop. In this context, the magnitude $|C_{bp}|$reflects the strength of the pressure-driven flow, while the sign indicates the reference-based normalization.

Fig. 17 plots the back-pressure coefficient C_{bp} as extracted from the CFD (using appropriate reference points: just in front of the rotor as upstream, and at the rotor exit plane for HAWT or diffuser exit for BDAWT as downstream) versus TSR = 4–10 for both configurations. In the HAWT, C_{bp} remains negative across the entire TSR range, since the rotor always causes a net pressure drop (suction) behind it by slowing the flow ($\mu < 1$ for all cases). As TSR increases from 4 to 7, the magnitude of this negative C_{bp} grows: at TSR 7, C_{bp} reaches a minimum of approximately -0.278. This corresponds to the point of strongest momentum extraction (maximal induction) in the HAWT, which we identified earlier as the optimal operating point. Beyond TSR 7, C_{bp} becomes less negative (rising to -0.20 at TSR 8, -0.15 at TSR 10, etc.). The reduction in $|C_{bp}|$ at high TSR is due to partial blade stall and the associated drop in lift and momentum capture, which means the rotor is not inducing as large a pressure drop as it did at TSR 7. By TSR 10, $C_{bp} \approx -0.116$ for the HAWT. The steepest change in C_{bp} occurs between TSR ≈6 and 8, which aligns well with the HAWT's peak performance window; this range marks the transition through the optimal induction and the onset of flow separation on the blades.

Conversely, in the BDAWT configuration, C_{bp} is positive for all examined TSRs and increases with TSR. For TSR = 4, C_{bp} is slightly above zero (indicating a small effective pressure rise when comparing diffuser exit to the free stream stagnation reference, likely because the diffuser exit pressure is slightly above the far field static pressure at that low rotor speed). As TSR increases, C_{bp} becomes substantially positive, reaching about $+0.40$ at TSR 7 and further to $+0.664$ at TSR = 10. This positive C_{bp} in the BDAWT stems from the diffuser's flow pre-acceleration and the strong static-pressure drop it generates at the exit (recall that in the diffuser case, we took the downstream point at the diffuser exit where pressure is lowest, and the upstream reference likely inside the diffuser inlet where pressure is slightly lower than free stream due to induction). A positive C_{bp} implies that the dynamic pressure term μ^2 more than offsets the static pressure drop in the normalized sense, in other words, the flow acceleration ($\mu > 1$) is so strong that the downstream dynamic pressure is higher relative to upstream, even though static pressure is lower. In simpler terms, the diffuser augmented turbine creates such a suction that it entrains additional mass flow and converts more pressure potential into kinetic energy in the wake. The slope of the C_{bp} curve for BDAWT is steep up to TSR ≈ 8 and then begins to taper off by TSR 10. This is consistent with our earlier observations: up to TSR 8, increasing rotor speed dramatically boosts the suction and flow augmentation (hence C_{bp} climbs quickly), but beyond TSR 8, turbulence losses and local flow separation in the diffuser's divergent section start to appear, which moderate further pressure drop (thus C_{bp} still rises from 8 to 10, but at a slower rate).

These back-pressure results provide another confirmation of the fundamental difference in how the two systems operate: the HAWT always operates by creating a decrease in the total pressure of the air (a "pressure drop" across the rotor), which corresponds to energy extracted. The BDAWT, on the other hand, due to the diffuser, can create a scenario where relative to the free-stream reference, the flow at the rotor plane and diffuser exit has higher dynamic pressure (hence the positive C_{bp}), highlighting the role of the diffuser in adding kinetic energy to the flow through guided acceleration. In practical terms, a high positive C_{bp} in the diffuser case correlates with higher thrust on the structure (since a large pressure difference across the system must be sustained), which implies the need for robust structural design, but it also means more energy is being harvested

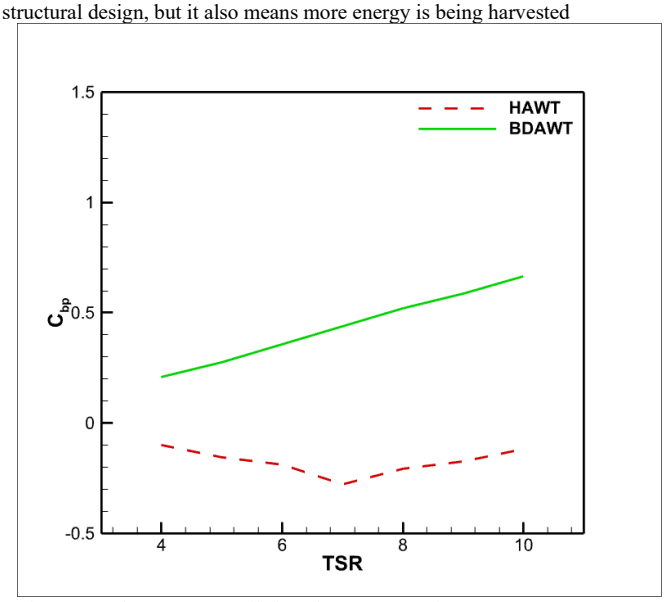

Fig. 17. Back-pressure coefficient for HAWT and BDAWT over TSR =4–10

To quantitatively assess loss mechanisms across operating conditions, representative area-averaged values of turbulent kinetic energy and wall shear stress were evaluated for both turbines over the range $TSR = 6 - 10$ and are summarized in Table 3. The turbulent kinetic energy represents an area-averaged value computed in the near wake region for the HAWT and in the diffuser and downstream wake region for the BDAWT, and it is normalized by the square of the free-stream velocity U_∞^2. Wall shear stress values correspond to surface-averaged quantities evaluated on the blade surfaces for the HAWT and on both the blade surfaces and the inner diffuser wall for the BDAWT; these values are normalized by their respective magnitudes at TSR = 7 to highlight relative changes with operating condition. Together, these metrics provide quantitative indicators of turbulence production, boundary layer behavior, and separation-related losses. The results show a gradual increase in turbulence from TSR = 6 to 8, followed by a pronounced rise in turbulent kinetic energy and a significant reduction in wall shear stress $at\ TSR = 9 - 10$, confirming the onset of separation-dominated losses at off design conditions.

Table 3. Quantitative indicators of turbulence and viscous losses for HAWT and BDAWT

Turbine	TSR	$\frac{TKE}{U_\infty^2}$	Wall shear stress (normalized)	Physical interpretation
HAWT	6	0.015	1.05	Fully attached flow, low losses
HAWT	7	0.018	1.00	Near-optimal operation
HAWT	8	0.022	0.95	Mild increase in turbulence
HAWT	9	0.026	0.82	Onset of partial blade stall
HAWT	10	0.031	0.70	Significant viscous and stall losses
BDAWT	6	0.019	1.08	Attached diffuser flow

Turbine	TSR	$\frac{TKE}{U_\infty^2}$	Wall shear stress (normalized)	Physical interpretation
BDAWT	7	0.022	1.00	Efficient pressure recovery
BDAWT	8	0.028	0.90	Near separation limit
BDAWT	9	0.038	0.65	Boundary-layer separation in diffuser
BDAWT	10	0.045	0.52	Strong separation and mixing losses

5. Conclusion

This work presented a detailed CFD investigation of a three-blade horizontal-axis offshore wind turbine (HAWT) versus a brimmed diffuser-augmented offshore wind turbine (BDAWT) over a range of TSR = 4–10, focusing on velocity fields, pressure distributions, and performance coefficients. Key findings from the study include:

Wake dynamics: In the HAWT, tip vortices form irregularly around and behind the rotor, leading to a broad wake with higher turbulence and energy loss. In the BDAWT, the diffuser and brim produce more organized vortex shedding (primarily at the brim), resulting in a narrower, more stable wake and improved aerodynamic performance.

Induction and velocity ratios: The HAWT's induction factor rises to a peak at TSR $\approx$ 7 then declines at higher TSR, whereas in the BDAWT it increases gradually up to TSR = 10. Correspondingly, the BDAWT's inlet (diffuser-exit) velocity ratio μ remains consistently higher than that of the HAWT across all TSRs, often exceeding unity ($\mu > 1$) confirming sustained flow acceleration through the rotor due to the diffuser.

Power coefficient: The HAWT achieved a maximum $CP \approx 0.39$ at its optimal $TSR \sim 7$. The BDAWT reached a significantly higher $CP \approx 0.59$, with its optimal TSR shifted to ~ 8 because the diffuser and brim augment the flow throughput and delay flow separation. Thus, the BDAWT captured substantially more power, even exceeding the classical Betz limit when referenced to rotor area. Practically, the shift of the optimal tip speed ratio from approximately 7 for the conventional HAWT to approximately 8 for the diffuser augmented turbine implies that the latter should be operated at a slightly higher rotational speed to achieve maximum efficiency. Accordingly, variable speed control strategies and drivetrain design parameters (e.g., torque, speed control laws or gear ratios) may need to be adapted to target $TSR \approx 8$. While this enables improved energy capture due to diffuser induced flow acceleration, potential impacts on blade loading and noise should also be considered in diffuser augmented turbine design.

Velocity and pressure profiles: The diffuser augmented turbine exhibited elevated axial velocities in the rotor region and at the exit (up to $\sim 25\%$ higher than free stream in the core flow), a strong low pressure (suction) zone at the diffuser throat and exit, delayed boundary layer separation on the blades, and a generally faster recovery of wind speed in the wake. The HAWT, by contrast, had a less pronounced velocity increase and a more diffuse low-pressure region, leading to a larger wake deficit. (Compared with the baseline HAWT, the brimmed diffuser pre accelerates the core flow by up to approximately 25% relative to the free stream velocity U_∞. This acceleration is caused by the diffuser induced pressure deficit at the exit, which enhances mass flow entrainment and increases the rotor plane velocity beyond the free stream value.)

Back pressure coefficient: The HAWT's back-pressure coefficient C_{bp} was negative (down to about -0.28 at optimal TSR), indicating the expected wake pressure drop. The BDAWT showed C_{bp}transitioning to positive values (up to $\sim +0.66$ at TSR 10), reflecting the diffuser's creation of extra suction and pre-acceleration of the flow. This highlights how the BDAWT is able to entrain additional energy from the flow that a HAWT cannot.

Collectively, these results demonstrate that a well-designed brimmed diffuser can enable a wind turbine to significantly surpass the performance of a conventional rotor by accelerating the incoming flow and stabilizing flow separation. In practical terms, the BDAWT can extract more energy from the wind (even beyond Betz's conventional limit) and maintain high efficiency over a wider range of operating conditions (TSRs). The quantitative insights provided by this study such as the detailed velocity and pressure distributions and the sensitivity of performance metrics to TSR offer concrete guidelines for optimizing diffuser geometries (angle, length, brim height) and selecting operational TSR ranges for diffuser-augmented turbines.

Moving forward, these CFD findings form a robust baseline for experimental validation. Future work will include wind tunnel or field testing of the BDAWT concept to verify the predicted gains in power coefficient and to assess structural and load implications of the increased thrust. Moreover, exploring different diffuser shapes and passive flow control devices (e.g., vortex generators on the diffuser) could further improve performance. The present study reinforces the potential of diffuser-augmented wind turbines to play a significant role in offshore wind energy, by enabling more compact turbines with higher power outputs, thereby contributing to more efficient renewable energy generation.

References

[1] Saidur R, Rahim NA, Islam MR, Solangi KH. Environmental impact of wind energy. Renew Sust Energy Rev. 2011;15(5):2423–2430.

[2] Manwell JF, McGowan JG, Rogers AL. Wind Energy Explained: Theory, Design and Application. Chichester: John Wiley & Sons; 2010.

[3] Ohya Y, Karasudani T. A shrouded wind turbine generating high output power with wind lens technology. Energies. 2010;3(4):634–649.

[4] Burton T, Jenkins N, Sharpe D, Bossanyi E. Wind Energy Handbook. Chichester: John Wiley & Sons; 2011.

[5] Betz A. Das Maximum der theoretisch möglichen Ausnützung des Windes durch Windmotoren. Z Gesamte Turbinenwes. 1920; 26:307–314.

[6] Paraschivoiu I. Wind Turbine Design: With Emphasis on Darrieus Concept. Montreal: Presses inter Polytechnique; 2002.

[7] Igra O. Research and development for shrouded wind turbines. Energy Convers Manage. 1981;21(1):13–48.

[8] Cresswell NW, Ingram GL, Dominy RG. The impact of diffuser augmentation on a tidal stream turbine. Ocean Eng. 2015; 108:155–163.

[9] Shahsavarifard M, Bibeau EL, Chatoorgoon V. Effect of shroud on the performance of horizontal axis hydrokinetic turbines. Ocean Eng. 2015; 96:215–225.

[10] El Zahaby AM, Kabeel AE, Elsayed SS, Obiaa MF. CFD analysis of flow fields for shrouded wind turbine's diffuser model with different flange angles. Alexandria Eng J. 2017;56(1):171–179.

[11] Dighe VV, de Oliveira G, Avallone F, van Bussel GJW. Characterization of aerodynamic performance of ducted wind turbines: A numerical study. Wind Energy. 2019;22(12):1655–1666.

[12] Ghenai C, Salameh T, Janajreh I. Modeling and simulation of shrouded horizontal axis wind turbine using RANS method. Jordan J Mech Ind Eng. 2017;11(4):279–288.

[13] Refaie AG, Hameed HSA, Nawar MA, Attai YA, Mohamed MH. Comparative investigation of the aerodynamic performance for several shrouded Archimedes-spiral wind turbines. Energy. 2022; 239:122295.

[14] Katooli MH, Noorollahi Y. Shrouded wind turbines: A critical review on research and development. Int J Ambient Energy. 2022;43(1):8775–8791.

[15] Hameed HSA, Hashem I, Nawar MA, Attai YA, Mohamed MH. Shape optimization of a shrouded Archimedean spiral type wind turbine for small scale applications. Energy. 2023; 263:125809.

[16] Du X, Yuan P, Tan J, Si X, Liu Y, Wang S, Lang X. Effects of support structure on the performance of a diffuser augmented hydrokinetic turbine. Ocean Eng. 2023; 285:115395.

[17] Mamouri AR, Khoshnevis AB, Lakzian E. Entropy generation analysis of S825, S822, and SD7062 offshore wind turbine airfoil geometries. Ocean Eng. 2019; 173:700–715.

[18] Mamouri AR, Khoshnevis AB, Lakzian E. Experimental study of the effective parameters on the offshore wind turbine's airfoil in pitching case. Ocean Eng. 2020; 198:106955.

[19] Mamouri AR, Lakzian E, Khoshnevis AB. Entropy analysis of pitching airfoil for offshore wind turbines in the dynamic stall condition. Ocean Eng. 2019; 187:106229.

[20] M. H. Katooli and Y. Noorollahi, "Shrouded wind turbines: a critical review on research and development," International Journal of Ambient Energy, vol. 43, no. 1, pp. 8775-8791, 2022.

[21] A. G. Refaie, H. A. Hameed, M. A. Nawar, Y. A. Attai, and M. H. Mohamed, "Comparative investigation of the aerodynamic performance for several Shrouded Archimedes Spiral Wind Turbines," Energy, vol. 239, p. 122295, 2022.

[22] H. S. A. Hameed, I. Hashem, M. A. Nawar, Y. A. Attai, and M. H. Mohamed, "Shape optimization of a shrouded Archimedean-spiral type wind turbine for small-scale applications," Energy, vol. 263, p. 125809, 2023.

[23] K. Watanabe and Y. Ohya, "A simple theory and performance prediction for a shrouded wind turbine with a brimmed diffuser," Energies, vol. 14, no. 12, p. 3661, 2021.

[24] X. Du et al., "Effects of support structure on the performance of a diffuser-augmented hydrokinetic turbine," Ocean Engineering, vol. 285, p. 115395, 2023.

[25] Hansen M. Aerodynamics of Wind Turbines. 3rd ed. Abingdon: Routledge; 2015.

[26] Anderson JD. Computational Fluid Dynamics: The Basics with

Applications. 2nd ed. New York: McGraw Hill; 2002.
[27] Pope SB. Turbulent Flows. Cambridge: Cambridge University Press; 2000.
[28] Ragheb M. Optimal rotor tip speed ratio. Lecture Notes, Course NPRE 475; University of Illinois; 2014.
[29] Leloudas SN, Lygidakis GN, Delis AI, Nikolos IK. Design optimization of shrouded wind turbines using an axisymmetric RANS BEM method and a differential evolution framework. SSRN Electron J. 2022. doi:10.2139/ssrn.4014185
[30] Ainley DG. Performance of axial flow turbines. Proc Inst Mech Eng. 1948;159(1):230–244.
[31] Watanabe K, Ohya Y. A simple theory and performance prediction for a shrouded wind turbine with a brimmed diffuser. Energies. 2021;14(12):3661.
[32] Aranake A, Duraisamy K. Aerodynamic optimization of shrouded wind turbines. Wind Energy. 2017;20(5):877–889.
[33] van Bussel GJW. The science of making more torque from wind: diffuser experiments and theory revisited. J Phys Conf Ser. 2007;75(1):012010.